Seo *et al. Energy Mater.* **2025**, *5*, 500123
DOI: 10.20517/energymater.2025.38

Energy Materials

Article

Open Access

Check for updates

Synergistic effect of cation substitution and *p*-type anion doping to improve thermoelectric properties in Zintl phases

Naeun Seo[1], Junsu Lee[1], Yunjeong Lee[1], Myung-Ho Choi[2], Ji Hee Pi[3], Kyu Hyoung Lee[3], Kang Min Ok[2], Tae-Soo You[1,*]

[1]Department of Chemistry, Chungbuk National University, Chungbuk 28644, Republic of Korea.
[2]Department of Chemistry, Sogang University, Seoul 04107, Republic of Korea.
[3]Department of Materials Science and Engineering, Yonsei University, Seoul 03722, Republic of Korea.

***Correspondence to:** Dr. Tae-Soo You, Department of Chemistry, Chungbuk National University, Cheongju, Chungbuk 28644, Republic of Korea. E-mail: tsyou@chungbuk.ac.kr

How to cite this article: Seo, N.; Lee, J.; Lee, Y.; Choi, M. H.; Pi, J. H.; Lee, K. H.; Ok, K. M.; You, T. S. Synergistic effect of cation substitution and *p*-type anion doping to improve thermoelectric properties in Zintl phases. *Energy Mater.* **2025**, *5*, 500123. https://dx.doi.org/10.20517/energymater.2025.38

Received: 16 Feb 2025 **First Decision:** 6 Apr 2025 **Revised:** 17 Apr 2025 **Accepted:** 8 May 2025 **Published:** 25 Jun 2025

Academic Editors: Yuping Wu, Sung Son Jae **Copy Editor:** Fangling Lan **Production Editor:** Fangling Lan

Abstract

Altogether, seven Zintl compounds in the solid solution $Ca_{9-x}Yb_xZn_{4.5-y}Cu_ySb_9$ ($0 \le x \le 1.5$, $0 \le y \le 0.15$) system were successfully prepared by the molten Pb-flux and hot-pressing method. From the powder X-ray and single crystal X-ray diffraction investigations, all these isotypic phases were observed to have been crystallized in the $Ca_9Mn_4Bi_9$-type phase (space group *Pbam*, Z = 2, Pearson code *oP*45). The overall crystal structure consists of complex anionic $[Zn_4Sb_9]$ clusters and the space-filling cationic elements. Notably, the central Zn1 site in a triangular coordinate exhibited a partial occupation and a relatively large atomic displacement parameter, which was necessary for the charge balance of the title compounds. All five intra-layer and inter-layer cationic sites showed the Ca/Yb mixed-occupancy with Yb presenting a specific site-preference for the A3 site. Density functional theory calculations unveiled a synergistic effect of the Yb-substitution and the *p*-type Cu-doping increased carrier concentration by reducing bond polarity through the tuning of the electronegativity difference. Thermoelectric property measurements further validated that the given synergistic effect was successful in enhancing the electrical conductivities of the quinary title compounds compared to the parental ternary compound $Ca_9Zn_{4.5}Sb_9$. As a result, the title compound $Ca_8YbZn_{4.4}Cu_{0.1}Sb_9$ achieved the largest figure-of-merit of 0.81 at 843 K, which should be attributed to improved electrical transport properties while maintaining balanced thermal conductivity.

Keywords: Zintl phase, thermoelectric materials, Yb-substitution, *p*-type Cu-doping

INTRODUCTION

Recent advancements in energy research have focused on developing sustainable solutions to address the global energy crisis[1]. Among these, thermoelectric (TE) materials hold a great deal of promise for directly converting waste heat into electrical energy[1,2]. The efficiency of such materials is typically evaluated using the figure-of-merit ZT, commonly defined as $ZT = \sigma S^2 T/\kappa$, where σ is the electrical conductivity, S is the Seebeck coefficient, T is the absolute temperature, and κ is the thermal conductivity[2]. As is obvious, a high σ, large S, and low κ are necessary to obtain an overall large ZT. Within the field of potential TE materials, Zintl phase compounds have garnered significant interest owing to their inherent semiconducting properties, complex crystal structures, and high thermal stabilities[3].

Over the last decade, our research team has tried to discover new Zintl phase systems and understand the correlation among the crystal structure, chemical compositions, and physical properties for TE applications. These phases includes the $A_{14}MSb_{11}$ (A = Ca, Yb; M = Al, Mg, Mn, Zn)[4,5], the AM_2Sb_2 (A = Ca, Sr, Ba, Eu, Yb; M = Zn, Cd)[6,7], the $Ca_9Cd_{3+x-y}M_{x+y}Sb_9$ (M = Cu, Zn)[8], and the $A_9M_{4+x}Sb_9$ (A = Ca, Eu, Yb; M = Mn, Zn, Cd) systems[9-11]. Among them, of particular interest is the $Ca_9Mn_4Bi_9$-type $A_9M_{4+x}Sb_9$ (A = Ca, Eu, Yb; M = Mn, Zn, Cd) systems[9-11]. Research on this system has been widely conducted all over the world owing to its considerably high ZT, and to enhance the ZT even further, many studies have explored various doping and substitution strategies on this system. However, the polymorphic feature of the "9-4-9" phase often produced some other "9-4-9" structure types rather than the targeted $Ca_9Mn_4Bi_9$-type phase[12], such as the three orthorhombic $Ca_9Mn_{4.41(1)}Sb_9$-type[13], $Eu_9Mn_{2.87(4)}Al_{1.13}Sb_9$-type[14], $Ca_{8.27}La_{0.73(1)}Mn_4Sb_9$-type phases[15], and the one hexagonal $Ca_9Zn_{3.1}In_{0.9}Sb_9$-type phase[16]. To address this issue, firstly, we attempted to apply the cation mixture using both Ca and Yb in the title system, which showed significant potential for enhancing ZT by increasing phonon scattering and reducing lattice thermal conductivity[17,18]. Secondly, in the $Ca_9Mn_4Bi_9$-type phase, interstitial M metal sites were found to significantly affect TE properties[19]. This suggests that adjusting the interstitial M metal content could enhance TE performance. Based on these findings, we hypothesized that p-type doping of Cu^+ for Zn^{2+} could increase charge carrier concentration, improve electrical conductivity, and eventually enhance TE performance. Thus, we investigated the synergetic effect of co-substitution using both cationic and anionic elements in the title $Ca_{9-x}Yb_xZn_{4.5-y}Cu_ySb_9$ system.

In this study, we successfully synthesized seven new compounds in the $Ca_{9-x}Yb_xZn_{4.5-y}Cu_ySb_9$ ($0 \le x \le 1.5$, $0 \le y \le 0.15$) system by the molten Pb-flux reaction method. A thorough analysis of the crystal structure using powder X-ray diffraction (PXRD) and single-crystal X-ray diffraction (SXRD) confirmed that all samples crystallized in the $Ca_9Mn_4Bi_9$-type phase. The distinct preference of cationic elements for one of the five available sites was explained by employing the electronic-factor criterion, derived from Q-values (QVAL) associated with individual atomic positions. Density functional theory (DFT) calculations using two structural models of $Ca_9Zn_{4.5}Sb_9$ and $Ca_8YbZn_4Cu_{0.5}Sb_9$ proved that the given structure type was flexible enough to accommodate a particular amount of p-type doping in the title system. To comprehend the electronic structure and observed TE properties, analyses were performed using the density of states (DOS), crystal orbital Hamilton population (COHP) curves, and electron localization function (ELF). The physical and chemical properties of the synthesized compounds were investigated by employing energy-dispersive X-ray spectroscopy (EDS), electron probe microanalysis (EPMA), and thermogravimetric analysis (TGA) techniques. Measurements of electrical transport properties and thermal conductivity demonstrated that substituting Yb for Ca effectively reduced κ_{tot}, while the p-type Cu-doping for Zn also increased σ, leading to an improved ZT. As a result, the quinary title compound $Ca_8YbZn_{4.4}Cu_{0.1}Sb_9$ finally attained the ZT of 0.81 at 843 K.

EXPERIMENTAL

Synthesis

Sample preparation was carried out within an argon-filled glovebox, where oxygen and moisture concentrations were kept below 0.1 ppm, or under vacuum. All reactants were bought from Alfa Aesar, and these included Ca (shot, 99.5%), Yb (ingot, 99.9%), Zn (shot, 99.99%), Cu (shot, 99.5%), Sb (shot, 99.9999%), and Pb (granules, 99.99%). The surfaces of Ca and Yb, which had become tarnished, were scrubbed using a metal brush inside an argon-filled glovebox before use. All reactant sets were introduced into alumina crucibles, accompanied by an excess quantity of Pb metal used as the metal-flux in the following ratios: Ca:Yb:Zn:Cu:Sb:Pb = 9:0:4.5:0:9:45, 8.5:0.5:4.5:0:9:45, 8:1:4.5:0:9:45, 7.5:1.5:4.5:0:9, 8:1:4.45:0.05:9:45, 8:1:4.4:0.1:9:45, and 8:1:4.35:0.15:9:45. Individual alumina crucibles were inserted into separate fused-silica tubes which were subsequently sealed under vacuum conditions to prevent oxidation of reactants during processing at elevated temperatures. Then, the reactants were annealed in a furnace ramped up to 1323 K at 200 K/h, kept there for 24 h, and then cooled down to 873 K at a rate of 5 K/h in 90 h. Afterward, the reaction ampoule was quickly taken out of the furnace and centrifuged for 3 min to separate the crystallized products from the molten Pb-metal flux. A small amount of remaining Pb metal after the centrifugation was further dissolved by soaking crystals in H_2O_2 for 48 h, and the needle/bar-shaped nicely grown single crystals were eventually obtained as shown in Figure 1.

Four of the title compounds were additionally prepared via ball-milling followed by a hot-pressing method to obtain larger quantities of samples suitable for TE property measurements. Initially, each reactant mixture corresponding to the target composition was placed into a stainless-steel container along with two 0.5-inch and two 0.25-inch stainless-steel balls inside an argon-filled glovebox. The mixtures were then ball-milled using a SPEX 8000M milling machine for 3 h. During this procedure, milling was paused every 30 min to scrape and thoroughly remix the powders, ensuring sample homogeneity. After completion of ball-milling, the resulting powdered products were consolidated into disk-shaped samples by hot-pressing under the following conditions: first at 623 K under 60 MPa for 2 h, and secondly at 1,073 K under the same pressure for an additional 2 h.

X-ray diffraction analysis

PXRD analysis was initially used to evaluate the phase purity of the five title compounds in the $Ca_{9-x}Yb_xZn_{4.5-y}Cu_ySb_9$ system ($0.57(2) \le x \le 1.28(2)$, $0 \le y \le 0.15$). The diffraction data were collected using a Bruker D8 diffractometer with monochromatic Cu $K_{\alpha 1}$ radiation (λ = 1.54059 Å). The data acquisition was conducted for 30 min per sample, utilizing a step size of 0.02°, covering the angular range of $20° \le 2\theta \le 80°$.

The phase purities were first examined by comparing the measured diffraction patterns with a calculated pattern based on the SXRD refinement results of $Ca_9Zn_{4.48(2)}Sb_9$; this comparison is shown in Figure 2. In addition, the Rietveld refinement was conducted for the collected PXRD patterns of three Zn/Cu mixture-containing quinary compounds using PDXL2 software to obtain the lattice parameters and volumes of the unit cells. The refinement results and lattice parameters are presented in Supplementary Table 1 and Supplementary Figure 1.

SXRD data was collected at room temperature for one ternary and three quaternary compounds: $Ca_9Zn_{4.48(2)}Sb_9$, $Ca_{8.42(2)}Yb_{0.57}Zn_{4.46(1)}Sb_9$, $Ca_{8.01(3)}Yb_{0.99}Zn_{4.46(1)}Sb_9$, and $Ca_{7.72(2)}Yb_{1.28}Zn_{4.45(2)}Sb_9$. The measurements were performed using a Bruker SMART APEX2 CCD-based diffractometer with Mo $K_{\alpha 1}$ radiation (λ = 0.71073 Å). Several single crystal specimens were initially screened for quality, and the most suitable specimen was selected for a thorough analysis using Bruker's APEX2 program[20]. Data reduction, integration, determination of unit cell parameters, and atomic site refinement were performed using the

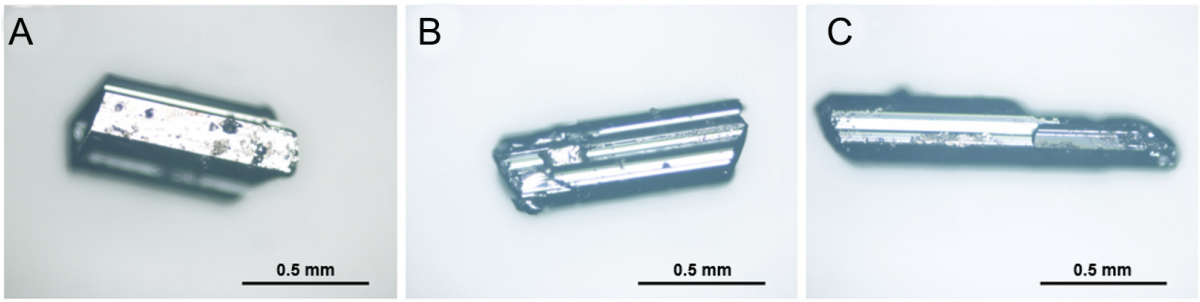

Figure 1. OM images for the needle/bar-shaped single-crystals of (A) $Ca_8YbZn_{4.45}Cu_{0.05}Sb_9$, (B) $Ca_8YbZn_{4.4}Cu_{0.1}Sb_9$, and (C) $Ca_8YbZn_{4.35}Cu_{0.15}Sb_9$. Scale bars are also provided.

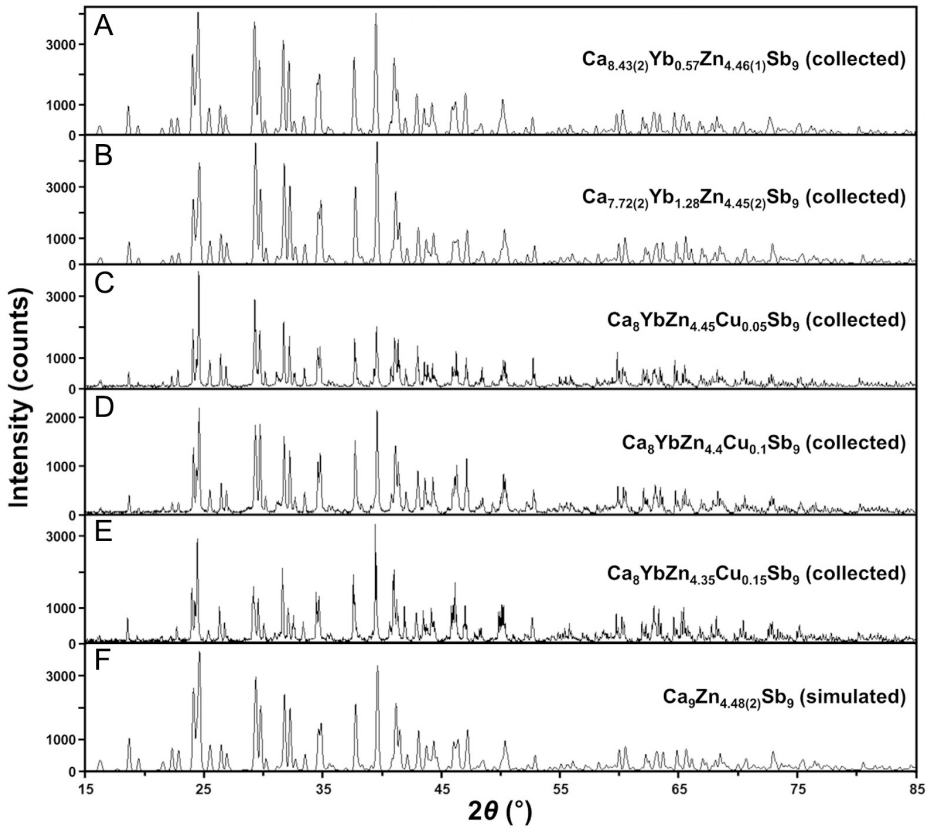

Figure 2. (A-F) PXRD patterns of five title compounds in the $Ca_{9-x}Yb_xZn_{4.5-y}Cu_ySb_9$ ($0.57(2) \le x \le 1.28(2)$, $0 \le y \le 0.15$) system. A PXRD pattern calculated from the SXRD data of $CaZn_{4.48(2)}Sb_9$ is also provided for a comparison purpose.

SAINT program[21]. Semi-empirical absorption corrections based on equivalents were applied using the SADABS program[22]. The entire reflection sets from these four products nicely matched with the orthorhombic *Pbam* space group (no. 55), and the isotypic crystal structures eventually crystallized in the $Ca_9Mn_4Bi_9$-type phase. The crystal structures were determined using a direct method and refined to convergence using full-matrix least-squares methods on F^2. The refinement included several parameters: the scale factor, atomic positions with anisotropic displacement parameters (ADPs), extinction coefficients, and occupancy factors for the Ca/Yb mixed sites. The STRUCTURE TIDY program[23] was employed for the standardization of atomic positions in the final refinement step. Comprehensive crystallographic data, atomic positions with ADPs, and selected interatomic distances are presented in Tables 1-3. All these

Table 1. Crystallographic data for $Ca_{9-x}Yb_xZn_{4.5-y}Sb_9$ [$0 \leq x \leq 1.28(2)$, $0.02(2) \leq y \leq 0.05(2)$] system

Empirical formula		$Ca_9Zn_{4.48(2)}Sb_9$	$Ca_{8.43(2)}Yb_{0.57}Zn_{4.46(1)}Sb_9$	$Ca_{8.01(3)}Yb_{0.99}Zn_{4.46(1)}Sb_9$	$Ca_{7.72(2)}Yb_{1.28}Zn_{4.45(2)}Sb_9$
Structure type		$Ca_9Mn_4Bi_9$-type			
Crystal system		Orthorhombic			
Space group		*Pbam* (No. 55)			
Lattice parameters (Å)	*a*	12.4557(6)	12.5080(3)	12.4546(4)	12.4523(7)
	b	21.848(1)	21.9140(6)	21.8344(6)	21.845(2)
	c	4.5425(2)	4.5574(1)	4.5412(1)	4.5438(2)
Volume ($Å^3$)		1,236.2(1)	1,249.18(5)	1,234.93(6)	1,236.0(2)
Density (g/cm^3)		4.700	4.847	5.058	5.151
Data/restraints/parameters		1,786/0/76	2,221/0/81	1,286/0/81	1,947/0/81
R indices[a] [$I > 2\sigma(I)$]	R_1	0.0198	0.0256	0.0194	0.0176
	wR_2	0.0402	0.0550	0.0383	0.0349
R indices[a] (all data)	R_1	0.0202	0.0291	0.0206	0.0223
	wR_2	0.0403	0.0565	0.0386	0.0364
Goodness of fit on F^2		1.406	1.199	1.264	1.065
Largest diff. of peak and hole ($e/Å^3$)		0.996/-1.350	0.930/-1.641	0.873/-1.329	0.883/-1.017

[a] $R_1 = \Sigma||F_o|-|F_c||/\Sigma|F_o|$; $wR_2 = \{\Sigma[w(F_o^2-F_c^2)/\Sigma[w(F_o^2)^2]]\}^{1/2}$, where $w = 1/[\sigma^2F_o^2+(A\text{-}P)^2+B\text{-}P]$, in which $P = (F_o^2 + 2F_c^2)/3$ and *A* and *B* are weight coefficients.

crystallographic data can be obtained free of charge from The Cambridge Crystallographic Data Centre via www.ccdc.cam.ac.uk/data_request/cif. The depository numbers are as follows: CCDC- 2422809 for $Ca_9Zn_{4.48(2)}Sb_9$, CCDC-2422810 for $Ca_{8.43(2)}Yb_{0.57}Zn_{4.46(1)}Sb_9$, CCDC- 2422811 for $Ca_{8.01(3)}Yb_{0.99}Zn_{4.46(1)}Sb_9$, and CCDC- 2422812 for $Ca_{7.72(2)}Yb_{1.28}Zn_{4.45(2)}Sb_9$.

DFT calculation

To understand how atomic substitutions influence the electronic structure of the studied system, DFT calculations were carried out by employing the TB-LMTO-ASA method[24-27] with two hypothetical models. For practical reasons, these two hypothetical models were designed to have the monoclinic subgroup *Pc* (no. 7) rather than the refined space group orthorhombic *Pnma* (no. 55) to apply the idealized compositions of $Ca_9Zn_{4.5}Sb_9$ and $Ca_8YbZn_4Cu_{0.5}Sb_9$. Lattice parameters and atomic sites information necessary to build these models were taken from the SXRD refinement results of $Ca_9Zn_{4.48(2)}Sb_9$ and $Ca_{8.01(3)}Yb_{0.99}Zn_{4.46(1)}Sb_9$, respectively. The obtained DOS, COHP curves, band structures, and ELF illustrations were carefully investigated. Detailed crystallographic information on these models is presented in Supplementary Table 2.

Table 2. Atomic coordinates, site occupancies, and equivalent isotropic atomic displacement parameters (U_{eq}[a]) for the $Ca_{9-x}Yb_xZn_{4-y}Sb_9$ ($0 \leq x \leq 1.28(2)$, $0.02(2) \leq y \leq 0.05(2)$) system

Atom	Wyckoff position	Occupancy	*x*	*y*	*z*	U_{eq}[a] (Å^2)
$Ca_9Zn_{4.48(2)}Sb_9$						
A1[b]	4*h*	1	0.0602(1)	0.4087(1)	$^1/_2$	0.0067(2)
A2[b]	4*h*	1	0.1223(1)	0.2391(1)	$^1/_2$	0.0090(2)
A3[b]	4*h*	1	0.3634(1)	0.3622(1)	$^1/_2$	0.0077(2)
A4[b]	4*g*	1	0.2891(1)	0.1026(1)	0	0.0115(2)
A5[b]	2*a*	1	0	0	0	0.0106(3)
Zn1	4*h*	0.24(1)	0.1042(3)	0.1029(2)	$^1/_2$	0.017(1)
Zn2	4*g*	1	0.2208(1)	0.4546(1)	0	0.0088(2)
Zn3	4*g*	1	0.3798(1)	0.2611(1)	0	0.0093(2)
Sb1	4*h*	1	0.1941(1)	0.0035(1)	$^1/_2$	0.0067(1)
Sb2	4*h*	1	0.3773(1)	0.1948(1)	$^1/_2$	0.0067(1)
Sb3	4*g*	1	0.0402(1)	0.1476(1)	0	0.0049(1)
Sb4	4*g*	1	0.1907(1)	0.3333(1)	0	0.0043(1)
Sb5	2*c*	1	0	0	0	0.0050(1)
$Ca_{8.43(2)}Yb_{0.57}Zn_{4.46(1)}Sb_9$						
A1[b]	4*h*	0.94(1)/0.06	0.0611(1)	0.4089(1)	$^1/_2$	0.0127(3)
A2[b]	4*h*	0.94(1)/0.06	0.1229(1)	0.2390(1)	$^1/_2$	0.0158(3)
A3[b]	4*h*	0.91(1)/0.09	0.3634(1)	0.3616(1)	$^1/_2$	0.0139(3)
A4[b]	4*g*	0.94(1)/0.06	0.2892(1)	0.1022(1)	0	0.0190(4)
A5[b]	2*a*	0.96(1)/0.04	0	0	0	0.0159(5)
Zn1	4*h*	0.23(1)	0.1044(4)	0.1026(2)	$^1/_2$	0.031(2)
Zn2	4*g*	1	0.2217(6)	0.4542(1)	0	0.0171(2)
Zn3	4*g*	1	0.3806(1)	0.2606(1)	0	0.0193(2)
Sb1	4*h*	1	0.1939(1)	0.0032(1)	$^1/_2$	0.0127(1)
Sb2	4*h*	1	0.3777(1)	0.1946(1)	$^1/_2$	0.0127(1)
Sb3	4*g*	1	0.0405(1)	0.1477(1)	0	0.0108(1)
Sb4	4*g*	1	0.1909(1)	0.3331(1)	0	0.0099(1)
Sb5	2*c*	1	0	$^1/_2$	0	0.0115(2)
$Ca_{8.01(3)}Yb_{0.99}Zn_{4.46(1)}Sb_9$						
A1[b]	4*h*	0.89(1)/0.11	0.06080(7)	0.40877(4)	$^1/_2$	0.0070(4)
A2[b]	4*h*	0.90(1)/0.10	0.12213(7)	0.23920(4)	$^1/_2$	0.0095(4)

A3[b]	4*h*	0.85(1)/0.15	0.36278(6)	0.36182(4)	$^1/_2$	0.0074(4)
A4[b]	4*g*	0.91(1)/0.09	0.28930(8)	0.10239(4)	0	0.0118(4)
A5[b]	2*a*	0.91(1)/0.09	0	0	0	0.0108(6)
Zn1	4*h*	0.23(1)	0.1049(3)	0.10319(16)	$^1/_2$	0.020(2)
Zn2	4*g*	1	0.22122(6)	0.45436(3)	0	0.0087(2)
Zn3	4*g*	1	0.38005(6)	0.26102(3)	0	0.0095(2)
Sb1	4*h*	1	0.19403(3)	0.00335(2)	$^1/_2$	0.0069(1)
Sb2	4*h*	1	0.37734(3)	0.19475(2)	$^1/_2$	0.0066(1)
Sb3	4*g*	1	0.04017(3)	0.14758(2)	0	0.0049(1)
Sb4	4*g*	1	0.19053(3)	0.33315(2)	0	0.0042(1)
Sb5	2*c*	1	0	$^1/_2$	0	0.0051(2)
$Ca_{7.72(2)}Yb_{1.28}Zn_{4.45(2)}Sb_9$						
A1[b]	4*h*	0.86(1)/0.14	0.0615(1)	0.4089(1)	$^1/_2$	0.0075(2)
A2[b]	4*h*	0.87(1)/0.13	0.1226(1)	0.2391(1)	$^1/_2$	0.0103(2)
A3[b]	4*h*	0.81(1)/0.19	0.3634(1)	0.3619(1)	$^1/_2$	0.0088(2)
A4[b]	4*g*	0.88(1)/0.12	0.2896(1)	0.1022(1)	0	0.0123(2)
A5[b]	2*a*	0.88(1)/0.12	0	0	0	0.0100(3)
Zn1	4*h*	0.23(1)	0.1054(3)	0.1035(2)	$^1/_2$	0.023(2)
Zn2	4*g*	1	0.2214(1)	0.4543(1)	0	0.0097(1)
Zn3	4*g*	1	0.3807(1)	0.2609(1)	0	0.0104(2)
Sb1	4*h*	1	0.1940(1)	0.0034(1)	$^1/_2$	0.0077(1)
Sb2	4*h*	1	0.3779(1)	0.1946(1)	$^1/_2$	0.0078(1)
Sb3	4*g*	1	0.0407(1)	0.1475(1)	0	0.0060(1)
Sb4	4*g*	1	0.1909(1)	0.3331(1)	0	0.0055(1)
Sb5	2*c*	1	0	$^1/_2$	0	0.0062(1)

[a]U_{eq} corresponds to one-third of the trace of the orthogonalized U_{ij} tensor; [b]A = Ca in $Ca_9Zn_{4.48(2)}Sb_9$; Ca/Yb mixed-site in the three quaternary compounds.

All relativistic effects were incorporated using a scalar relativistic approximation, except for spin-orbit coupling. The potential inside each Wigner-Seitz (WS) sphere was treated as spherically symmetric[28], and a combined correction was applied to account for the overlapping regions. Empty spheres were automatically included, and the space was filled with overlapping WS atomic spheres[28]. The WS sphere radii were automatically calculated to optimize the overlapping potential's approximation to the full potential. The WS radii used for the two models are as follows: Ca, 1.891-2.158 Å; Zn, 1.335-1.504 Å; Sb, 1.631-1.911 Å for $Ca_9Zn_{4.5}Sb_9$; Ca, 1.891-2.158 Å; Yb, 1.975-2.040 Å; Zn, 1.335-1.504 Å; Cu, 1.465 Å; Sb, 1.631-1.911 Å for $Ca_8YbZn_4Cu_{0.5}Sb_9$. The used basis sets were 4s, 4p and 3d orbitals for Ca, 6s, 6p and 5d orbitals for Yb, 4s, 4p and 3d orbitals for Zn, 4s, 4p and 3d orbitals for Cu, 5s, 5p, 5d and 4f orbitals for Sb. The

Table 3. Selected bond distances for the $Ca_{9-x}Yb_x Zn_{4-y}Sb_9$ [$0 \leq x \leq 1.28(2)$, $0.02(2) \leq y \leq 0.05(2)$] system

Atomic pair	Bond distance (Å)			
	$Ca_9Zn_{4.48(2)}Sb_9$	$Ca_{8.43(2)}Yb_{0.57}Zn_{4.46(1)}Sb_9$	$Ca_{8.01(3)}Yb_{0.99}Zn_{4.46(1)}Sb_9$	$Ca_{7.72(2)}Yb_{1.28}Zn_{4.45(2)}Sb_9$
A1[a] - Sb1	3.695(2)	3.696(1)	3.686(1)	3.6784(7)
A1[a] - Sb2	3.211(2)	3.226(1)	3.214(1)	3.2159(7)
A1[a] - Sb4	3.2426(7)	3.2543(7)	3.239(1)	3.2407(5)
A1[a] - Sb5 (×2)	3.1140(7)	3.1239(6)	3.114(1)	3.1162(4)
A2[a] - Sb2	3.377(2)	3.394(2)	3.373(1)	3.3729(8)
A2[a] - Sb3	3.1937(7)	3.2036(7)	3.194(1)	3.1939(5)
A2[a] - Sb4	3.1817(7)	3.1884(7)	3.176(1)	3.1782(5)
A3[a] - Sb1	3.169(2)	3.184(1)	3.170(1)	3.1737(7)
A3[a] - Sb3 (×2)	3.1712(8)	3.1846(6)	3.175(1)	3.1743(5)
A3[a] - Sb4	3.1909(8)	3.1998(7)	3.186(1)	3.1889(5)
A4[a] - Sb1	3.3546(8)	3.3638(8)	3.353(1)	3.3515(6)
A4[a] - Sb2	3.2282(8)	3.2435(8)	3.229(1)	3.2329(5)
A4[a] - Sb5 (×2)	3.454(2)	3.459(2)	3.447(1)	3.4421(7)
A5[a] - Sb1	3.3177(3)	3.3287(3)	3.353(1)	3.3174(3)
Zn1 - Sb1	2.444(3)	2.450(3)	2.446(4)	2.450(3)
Zn1 - Sb3 (×2)	2.597(2)	2.608(2)	2.597(2)	2.595(2)
Zn2 - Sb1 (×2)	2.7245(4)	2.7315(4)	2.723(1)	2.7241(4)
Zn2 - Sb4	2.6755(7)	2.6808(8)	2.674(1)	2.6749(7)
Zn2 - Sb5 (×2)	2.9243(6)	2.9492(8)	2.930(1)	2.9329(6)
Zn3 - Sb2 (×2)	2.6939(4)	2.6997(5)	2.693(1)	2.6945(4)
Zn3 - Sb3	2.8231(7)	2.8356(8)	2.821(1)	2.8218(7)
Zn3 - Sb4	2.8352(7)	2.8558(9)	2.838(1)	2.8400(7)

[a]A: Ca in $Ca_9Zn_{4.48(2)}Sb_9$; Ca/Yb mixed-site in the three quaternary compounds.

Löwdin downfolding technique[29] was employed for the Ca 4p, Yb 6p, and Sb 5d and 4f orbitals. Integration in *k*-space was performed using the tetrahedron method, and the self-consistent charge density was computed across the first Brillouin zone using 320 irreducible *k*-points for both models[30].

TGA

The TGA, performed on a Netzsch TG 209 F1 Libra instrument, was utilized to evaluate the thermal stability of three synthesized compounds. Each pulverized sample (around 20 mg) was positioned in an alumina pan. Heating proceeded to 1,123 K under a constant nitrogen flow, with the temperature ramped at 10 K/min. Following the heating cycle, the samples underwent natural cooling back to ambient temperature. The resulting TGA curves [Supplementary Figure 2] indicated that the three compounds maintained thermal integrity up to roughly 900 K.

Electrical transport property measurement

First, disk-shaped specimens were prepared using a two-step pressing process: initial hot-pressing at 623 K for 2 h under 60 MPa, followed by pressing at 1,073 K for 2 h. From these disks, square bars (3 mm × 3 mm × 10 mm) were cut and polished for the electrical measurements. It was verified through geometric density checks that all samples achieved densities above 96%. Under a helium atmosphere, the temperature-dependent electrical conductivity σ and Seebeck coefficient S of the four compounds were measured simultaneously from 323 to 861 K with a ULVAC-RIKO ZEM-3 system.

Thermal conductivity measurement

Using the flash diffusivity method, thermal diffusivity was evaluated for the four disk-shaped title compounds between 323 and 861 K. The measurements were performed with a Netzsch LFA 467 HyperFlash system in an argon environment, where a laser pulse heats the sample's front surface, and an Infrared (IR) detector tracks the subsequent temperature rise on the back surface. The thermal conductivity κ was determined using $\kappa = DC_p\rho$, where D = thermal diffusivity, C_p = heat capacity, and ρ = density[31]. The Dulong-Petit value ($3R$/atom, R = gas constant) was used for C_p[31]. The total thermal conductivity κ_{tot} was calculated by the sum of the lattice κ_{latt} and the electronic κ_{elec} thermal conductivities[32]. The electronic thermal conductivity was evaluated using the Wiedemann-Franz law: $\kappa_{elec} = L\sigma T$, where L is the temperature-dependent Lorenz number, which was derived from the single-parabolic band model using the temperature-dependent Seebeck coefficient S[32]. Subsequently, the lattice thermal conductivity was calculated using: $\kappa_{latt} = \kappa_{tot} - \kappa_{elec}$.

EDS and EPMA analysis

The elemental composition and distribution within the compounds $Ca_8YbZn_{4.35}Cu_{0.05}Sb_9$, $Ca_8YbZn_{4.4}Cu_{0.1}Sb_9$, and $Ca_8YbZn_{4.35}Cu_{0.15}Sb_9$ were investigated using EDS. The measurements were carried out using a ULTRA Plus FE-SEM, with the operating condition set to an acceleration potential of 20 kV. Well-grown single crystals synthesized via the molten Pb-flux technique were affixed to an aluminum sample holder under an argon atmosphere. Results from the EDS analysis, presented in Supplementary Figure 3, indicated a homogeneous distribution of Cu within these single crystals. In particular, the quantitative elemental analyses of these three title compounds were also conducted by the JEOL JXA-IHP200F EPMA using an acceleration voltage of 20 KeV with a current of 50 nA in a WDS mode for randomly selected locations. EPMA analysis resulted in the chemical compositions of $Ca_{8.25}Yb_{0.86}Zn_{4.51}Cu_{0.07}Sb_{8.81}$, $Ca_{8.36}Yb_{1.00}Zn_{4.49}Cu_{0.11}Sb_{8.54}$, and $Ca_{8.11}Yb_{1.01}Zn_{4.54}Cu_{0.14}Sb_{8.69}$ for $Ca_8YbZn_{4.45}Cu_{0.05}Sb_9$, $Ca_8YbZn_{4.4}Cu_{0.1}Sb_9$, and $Ca_8YbZn_{4.35}Cu_{0.15}Sb_9$, respectively.

RESULTS AND DISCUSSION

Crystal structure analysis

Seven title compounds in the $Ca_{9-x}Yb_xZn_{4.5-y}Cu_ySb_9$ ($0 \le x \le 1.50$, $0 \le y \le 0.15$) system were prepared using the molten Pb-flux method. Initial structural assessments, including the determination of phase purities and lattice parameters of all compounds, were conducted through Rietveld refinements for the collected PXRD data. As displayed in Figure 2 and Supplementary Figure 1, all seven compounds crystallize as single-phase products. The refined lattice parameters were consistent with those obtained from SXRD data refinement. Further detailed structural refinements for one ternary and three quaternary Zn-containing title compounds were conducted by SXRD analysis, and the resultant crystallographical details are listed in Tables 1-3. The studied compounds adopted the $Ca_9Mn_4Bi_9$-type phase having an orthorhombic *Pbam* space group (Pearson code *oP*44, Z = 2)[13], and thirteen crystallographically independent atomic sites including the five Ca or Ca/Yb mixed-sites, three Zn or Zn/Cu mixed-sites, and five Sb sites were refined and presented in Table 2. However, the detailed chemical compositions of the three quinary compounds containing both Zn and Cu were not accurately refined using SXRD data since X-ray scattering factors of Zn and Cu were similar. Instead, the detailed chemical compositions of these compounds were evaluated by EPMA analysis, and the results are as follows: $Ca_{8.25}Yb_{0.86}Zn_{4.51}Cu_{0.07}Sb_{8.81}$, $Ca_{8.36}Yb_{1.00}Zn_{4.49}Cu_{0.11}Sb_{8.54,}$ and $Ca_{8.11}Yb_{1.01}Zn_{4.54}Cu_{0.14}Sb_{8.69}$ for $Ca_8YbZn_{4.45}Cu_{0.05}Sb_9$, $Ca_8YbZn_{4.4}Cu_{0.1}Sb_9$, and $Ca_8YbZn_{4.35}Cu_{0.15}Sb_9$ (all nominal compositions).

Since all seven title compounds are isostructural, the detailed overall crystal structure can be explained using a representative quaternary compound $Ca_{8.43(2)}Yb_{0.57}Zn_{4.46(1)}Sb_9$ in Figure 3. The presented crystal arrangement can basically be elucidated as an assembly of (1) a complex 2-dimensional (2D) layered anionic structure; and (2) two different types of electron-donating cationic elements. Interestingly, the 2D anionic layered

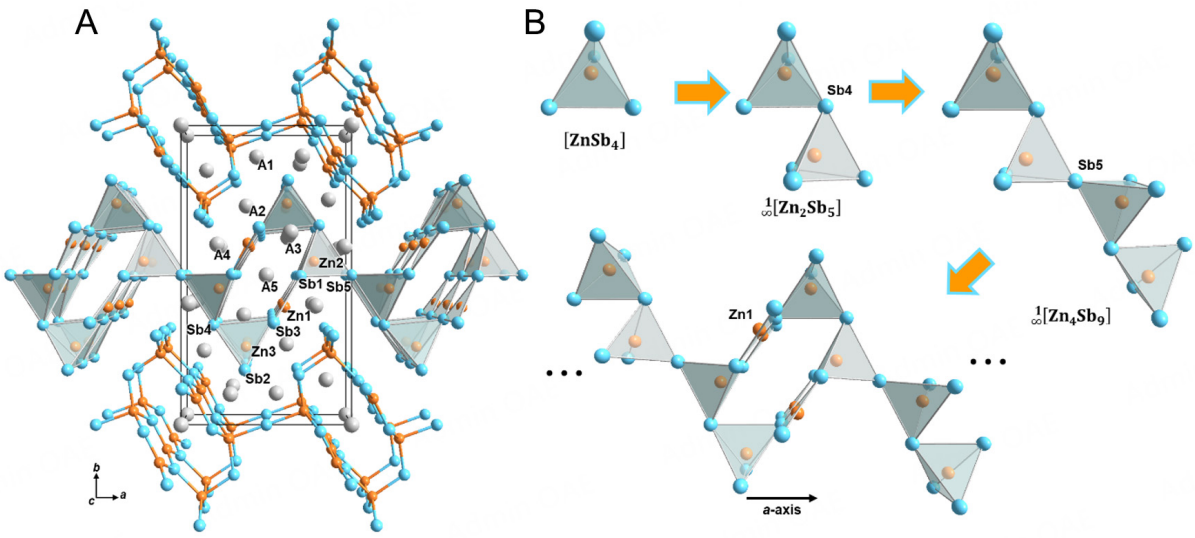

Figure 3. (A) A crystal structure of $Ca_{8.43(2)}Yb_{0.57}Zn_{4.46(1)}Sb_9$ illustrated by a combination of ball-and-stick and polyhedral representations viewed down from the *c*-axis direction. (B) A schematic presentation of the assembly of the 2D anionic layered structure. Color codes: A (Ca/Yb mixed-site): gray; Zn: orange; Sb: blue.

structure can be built up from its basic building block of the $[ZnSb_4]$ tetrahedron, which initially forms the 1D $^1_\infty[ZnSb_3]$ chains propagating along the *c*-axis direction by sharing Sb2 with its neighboring tetrahedra [Figure 3B]. These 1D chains are linked together via Sb4 to build the $^1_\infty[Zn_2Sb_5]$ double chains. Then, two such double chains are further joined via Sb5 in the form of the inversion symmetry resulting in building the $^1_\infty[Zn_4Sb_9]$ cluster.

Finally, these anionic clusters are connected to one another via the bridging Zn1 along the *a*-axis directions to complete the complete 2D layered structure. In particular, these two different types of Zn sites were refined in this anionic framework with distinctive local coordination geometries and different occupations: (1) the Zn1 site (Wyckoff 4*h*) was located at the center of the trigonal planar site with a partial occupation of *ca*. 24%; and (2) the Zn2 and Zn3 (both Wyckoff 4*g*) were found to be at the center of the tetrahedral site with full occupations. Interestingly, the Zn1 site showed a rather larger atomic displacement parameter (ADP) value than two other Zn sites as given in Table 2. This kind of large ADP value was already reported in other isotypic $Ca_9Mn_4Bi_9$-type compounds, including $Ca_9Zn_{4.10(1)}Bi_9$, $Sr_9Cd_{4.49(1)}Sb_9$, $Ca_9Zn_{4.478(8)}Sb_9$, and $Yb_9Zn_{4.380(12)}Sb_9$[33,34]. Thus, it can be considered as an intrinsic structural feature of the title phase due to the partial Zn1 occupation. Furthermore, based on the Zintl-Klemm concept, we could rewrite the chemical formula of the title compounds as: $[(Ca/Yb)^{2+}]_{18}[(4b\text{-}Zn^{2-})_8(3b\text{-}Zn^{1-})(1b\text{-}Sb^{2-})_3(2b\text{-}Sb^{1-})_{13}(3b\text{-}Sb^0)_2]$. Therefore, we believe that the 1/4 occupation at the Zn1 site as shown in the formula should occur to optimize the overall charge balance between cations and anions. In addition, the charge balance evaluation based on the coordination geometry is also nicely supported by the ELF analysis, which will be explained further in the Electronic Structure Analysis section.

Five different types of cationic sites existed in the title system (See Figure 4): (1) the two intra-layer A3 and A5 sites located inside the "channel-like" voids within the anionic 2D layers; and (2) the three inter-layer A1, A2, and A4 sites situated in-between two such neighboring 2D layers as displayed in Figure 3. All these cationic sites were primarily coordinated by six Sb, which formed a slightly distorted octahedral geometry, and depending on the given local coordination environment, some of the triangular faces were capped by

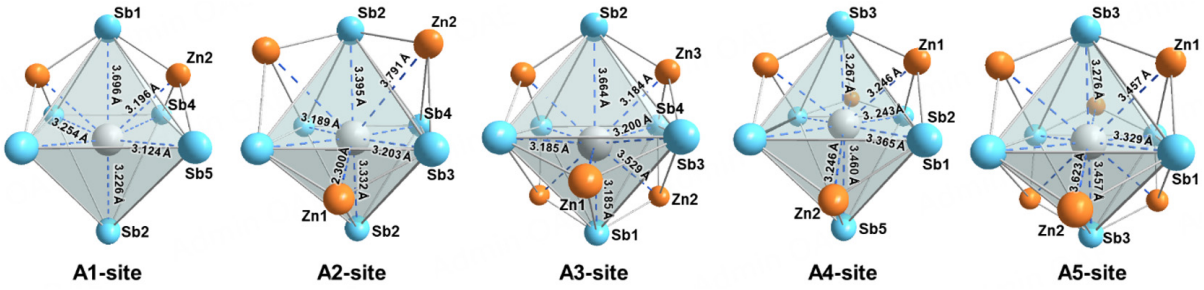

Figure 4. Illustration of the five distinct cationic environments identified within the $Ca_{8.43(2)}Yb_{0.57}Zn_{4.46(1)}Sb_9$ structure. Detailed labeling of atoms and chosen interatomic distance are also shown.

Zn atoms resulting in the various site volumes. Interestingly, in the two quaternary compounds having the Ca/Yb mixed-sites, Yb showed a specific affinity for the A3 site among the five possible cationic sites.

The observed site-preference behavior is typically influenced by one of the following main factors: (1) the size factor, which reflects the compatibility between the central cation and the site volume; or (2) the electronic factor represented by the QVAL[17], which is the relationship between the electronegativity of a cation and an electron density at the site. In our title system, the difference in size between two divalent cations Ca^{2+} and Yb^{2+} is quite subtle [$r(Ca^{2+})$ = 1.00 Å and $r(Yb^{2+})$ = 1.02 Å][35]. Consequently, the electronic factor should be considered the determining criterion for Yb's observed preference for the A3 site. A detailed analysis of the correlation between the electronic factor and cationic site-preference will be a part of the Electronic Structure section.

Electronic structure and chemical bonding analysis

To understand how the co-substitution of Yb for Ca and Cu for Zn affects the electronic structure of the $Ca_{9-x}Yb_xZn_{4.5-y}Cu_ySb_9$ system, DFT calculations using the TB-LMTO-ASA method were performed[24-27]. Therefore, two hypothetical structural models containing only Yb or both Yb and Cu were systematically designed with the idealized compositions of $Ca_8YbZn_{4.5}Sb_9$ and $Ca_8YbZn_4Cu_{0.5}Sb_9$, and their electronic structures were calculated and compared with that of the parental compound $Ca_9Zn_{4.5}Sb_9$. To incorporate these specific compositions and atomic arrangements in the models, the symmetry was reduced from the experimentally refined space group *Pbam* (no. 55), which contains 13 crystallographically independent atomic sites, to its subgroup *Pc* (no. 7), which contains 48 atomic sites. In particular, three out of four Zn1 sites were treated as vacancies to mimic the partial occupation observed in the SXRD refinements. For the quinary $Ca_8YbZn_4Cu_{0.5}Sb_9$ model, Cu with a higher electronegativity than Zn was assigned to partially occupy the Zn2 site (Wyckoff 4*g* site) showing the largest QVAL amidst the three available Zn sites. Additional crystallographic details, including lattice parameters and atomic coordinates, were obtained from the SXRD results of $Ca_9Zn_{4.48(2)}Sb_9$ and $Ca_{8.01(3)}Yb_{0.99}Zn_{4.46(1)}Sb_9$, respectively. Supplementary Table 2 presents further details for the two studied hypothetical models.

The calculated total DOS (TDOS) and partial DOS (PDOS) curves of $Ca_9Zn_{4.5}Sb_9$ and $Ca_8YbZn_4Cu_{0.5}Sb_9$ resembled each other since they adopted the identical $Ca_9Mn_{4.5}Bi_9$-type crystal structure [Figure 5A]. Strong orbital mixing among all elements was observed across the entire energy window, and the pseudogap noted at the Fermi level (E_F) was indicative of the poor metallic properties of these title compounds. In particular, the slightly increased metallic properties should be expected for the *p*-type Cu-substituting compounds since, as shown in Figure 5B, the DOS level at E_F increased in the $Ca_8YbCu_{0.5}Sb_9$ model. In addition, the wide *p*-orbital states ranging between *ca.* -6.5 and 0 eV can be interpreted by dividing into two sub-sections: (1) the lower section between *ca.* -6.5 and -4.5 eV, where Zn2 and Zn3 showed relatively larger contributions;

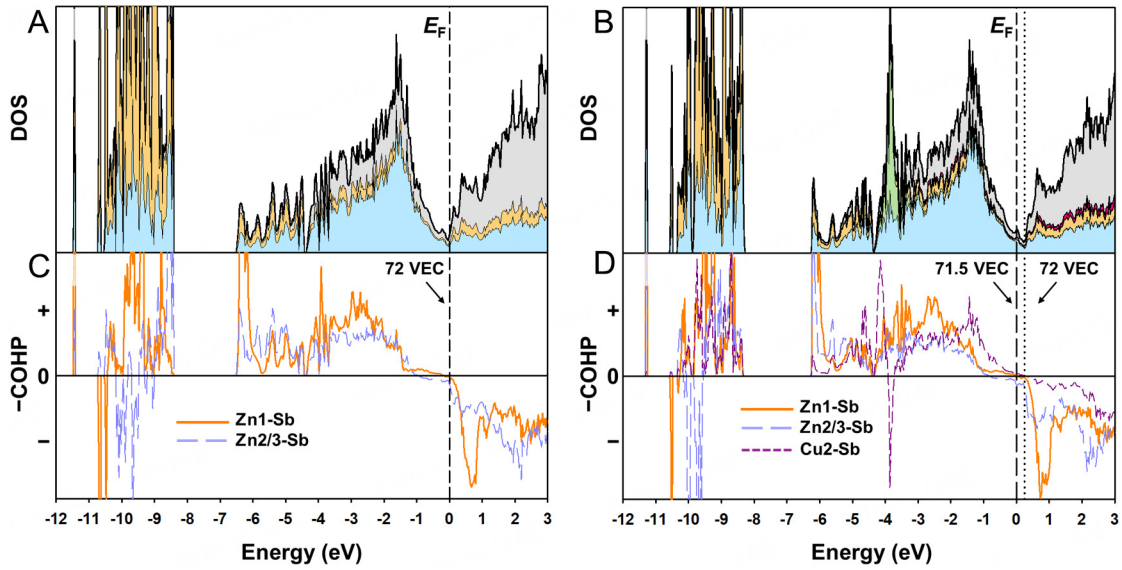

Figure 5. TDOS, PDOS and COHP curves of $Ca_9Zn_{4.5}Sb_9$ (A, C) and $Ca_8YbZn_4Cu_{0.5}Sb_9$ (B, D). The E_F corresponding to 72 and 71.5 valence electron count (VEC) in (A and B) is set as the reference energy (0 eV) and marked with a dashed vertical line. An additional line corresponding to 72 VEC in (B) is shown with a dotted line. In the COHP diagram, "+" regions indicate bonding interactions, while "-" regions represent antibonding interactions. Color codes in DOS curves are as follows: TDOS: bold black outline; Ca PDOS: gray region; Yb PDOS: magenta region; Zn TDOS: yellow region; Cu PDOS: green region; Sb PDOS: sky blue region.

and (2) the higher section between *ca.* -4.5 and 0 eV, where Zn1 displayed a relatively stronger contribution. Two or three COHP curves were evaluated to represent the averaged interatomic interactions between Zn and Sb atoms either in a triangular environment of the [$ZnSb_3$] unit or in the tetrahedral coordination of the [$ZnSb_4$] unit [See Figure 5C and D]. In particular, the Cu2-Sb COHP curve in the quinary $Ca_8YbZn_4Cu_{0.5}Sb_9$ model was also displayed in Figure 5D. Overall, both of these types of Zn-Sb and Cu-Sb COHP curves were nicely optimized at E_F in both structural models, and the non-bonding characteristics continued even below E_F indicating the possibility of a certain amount of *p*-type doping on the anionic sites. However, above E_F, these two Zn-Sb interactions showed quite strong antibonding characteristics. In particular, the Zn1-Sb COHP curves displayed a three-fold stronger antibonding character than that of Zn2/3-Sb. This strongly indicated that the central site of the [$ZnSb_3$] triangle was supposed to be partially occupied as experimentally observed in the SXRD refinement results.

The ELF calculations were conducted as well for these two structural models to analyze the different distributions of lone-pairs of electrons on the bridging Sb4 in two structural models. As shown in Figure 6, two lone-pairs of electrons on Sb4 merged together producing the "C-shaped" electron densities. In addition, due to the stronger electron withdrawing ability of Cu than Zn, these lone-pairs in the Cu-containing compound shown in Figure 6B were further spread out toward the Cu-substituents in $Ca_8YbZn_4Cu_{0.5}Sb_9$. In general, this kind of substitution can affect the bond polarity on the anion frameworks. Given the electronegativity difference among anionic elements (Zn = 1.65, Cu = 1.90, and Sb = 2.05 in the Pauling scale)[36], as Cu was introduced, the bond polarity of the Cu-Sb became smaller than that of Zn-Sb. As the bond polarity decreases, the particular bond becomes relatively more flexible, which leads to the high doping efficiency and the corresponding high carrier concentration[37]. This enhancement in carrier concentration contributes to improved electrical conductivity, which eventually improves the electrical conductivity based on $\sigma = ne\mu$, where σ = electrical conductivity, n = carrier concentration, e = the charge of an electron, μ = carrier mobility[6]. Detailed discussion will be discussed in the following Thermoelectric Properties section.

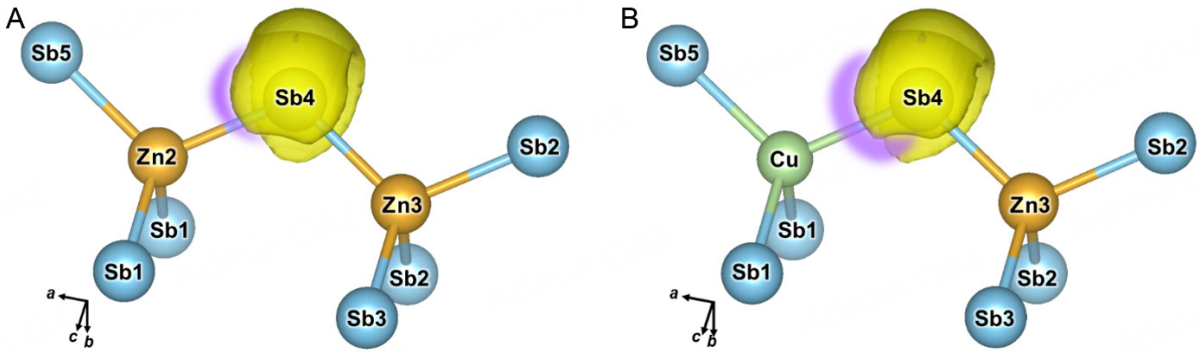

Figure 6. ELF analysis illustrating the electron lone-pairs associated with the bridging Sb4 in (A) $Ca_9Zn_{4.5}Sb_9$ and (B) $Ca_8YbZn_4Cu_{0.5}Sb_9$. The 3D isosurfaces identify regions where the ELF values are higher than 0.59.

To understand the affinity of Yb for the A3 site, the QVAL of the five cationic sites in the ternary $Ca_9Zn_{4.5}Sb_9$ model was thoroughly evaluated by integrating electron densities within each corresponding WS sphere. As briefly mentioned in the previous section, in the Yb-containing quaternary compounds, Yb showed a discernible site-preference for the A3 site. This site-preference of any component is generally governed by two factors: (1) the size factor criterion taking into account the compatibility between the site volume and the size of the occupying element; and (2) the electronic factor criterion determined by the relationship between the intrinsic QVAL of each atomic site and the electronegativity of an occupying element. We thoroughly investigated those two factors to study the site preference of Yb and concluded that since Ca^{2+} and Yb^{2+} possess quite similar effective ionic radii (1.00 and 1.02 Å, respectively)[35], any size-based preference could not be considered as a deciding factor. On the other hand, as presented in Table 4, the site with the highest QVAL of 2.336 is the A3 site. Therefore, this particular site should be preferred by the more electronegative Yb (Ca = 1.04, Yb = 1.06 on the Allred-Rochow scale)[36].

Thermoelectric properties measurements

To investigate the effects of cationic substitution with divalent Yb and anionic *p*-type substitution with monovalent Cu, the temperature-dependent TE properties were measured across a temperature range of 323 to 861 K.

First, Figure 7A shows the temperature-dependent electrical conductivities σ of four title compounds. All compounds exhibited decreasing electrical conductivity σ with increasing temperature which is a characteristic typical of a heavily doped degenerate semiconductor. The measured σ values at 323 K were 243.4, 434.1, 542.8, 567.9, and 430.4 S/cm for $Ca_9Zn_{4.5}Sb_9$[19], $Ca_8YbZn_{4.5}Sb_9$, $Ca_8YbZn_{4.45}Cu_{0.05}Sb_9$, $Ca_8YbZn_{4.4}Cu_{0.1}Sb_9$, and $Ca_8YbZn_{4.35}Cu_{0.15}Sb_9$, respectively.

In particular, the σ values were higher in one quaternary compound with the Yb substitution and three quinary compounds with the Yb and Cu co-substitution compared to in the ternary parental compound $Ca_9Zn_{4.5}Sb_9$. This type of improvement of σ can be ascribed to the increased hole concentration in the quaternary and quinary compounds having the Yb and Cu substitutions as shown in Table 5.

The temperature-dependent Seebeck coefficients *S* of the title compounds are displayed in Figure 7B. The *S* values in all studied cases increased with temperature up to *ca.* 700 K, and then the values were saturated beyond 700 K. The maximum *S* values were 149.9, 163.2, 125.5, 144.5, and 147.2 μV/K for $Ca_9Zn_{4.5}Sb_9$[19], $Ca_8YbZn_{4.5}Sb_9$, $Ca_8YbZn_{4.45}Cu_{0.05}Sb_9$, $Ca_8YbZn_{4.4}Cu_{0.1}Sb_9$, and $Ca_8YbZn_{4.35}Cu_{0.15}Sb_9$, respectively. The quaternary compound $Ca_8YbZn_{4.5}Sb_9$ showed the highest *S*, which typically showed the opposite trend to

Table 4. QVAL and volume of the five cationic sites in $Ca_9Zn_{4.5}Sb_9$

Atom (Wyckoff site)	Ca1 (4*h*)	Ca2 (4*h*)	Ca3 (4*h*)	Ca4 (4*g*)	Ca5 (2*a*)
QVAL	1.800	2.279	2.336	2.312	2.215
Volume ($Å^3$)	50.82	57.80	63.72	62.29	73.17

Table 5. Hall effect measurement results for the three title compounds

Compound	Carrier concentration *n* (× 10^{20} carriers/cm^3)	Mobility η (cm^2/V·s)
$Ca_9Zn_{4.5}Sb_9$[19]	0.607	48.966
$Ca_8YbZn_{4.5}Sb_9$	0.663	47.705
$Ca_8YbZn_{4.4}Cu_{0.1}Sb_9$	0.700	28.864
$Ca_8YbZn_{4.35}Cu_{0.15}Sb_9$	1.264	23.755

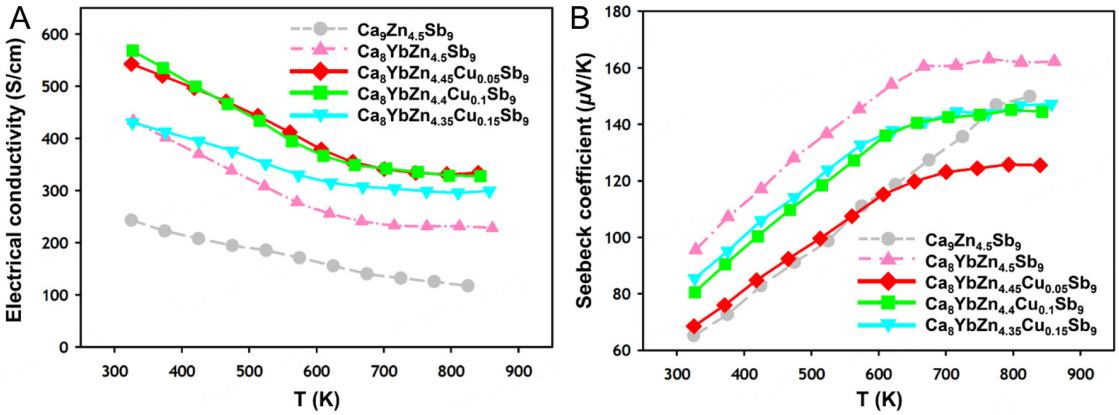

Figure 7. For four compounds in the $Ca_8YbZn_{4.5-y}Cu_ySb_9$ ($0 \le y \le 0.15$) system, temperature-dependent (A) electrical conductivity σ and (B) Seebeck coefficient *S* are plotted over the range of 323 to 861 K. Corresponding data for the ternary $Ca_9Zn_{4.5}Sb_9$[19] compound are presented for comparison.

those of σ. In general, the correlation between *S*, the carrier concentration, and the effective mass can be expressed by = $\frac{8\pi^2 k_B^2}{3eh^2} m^* T (\frac{\pi}{3n})^{\frac{2}{3}}$, where k_B = the Boltzmann constant, *e* = the charge of electron, *h* = the Planck constant, *n* = the carrier concentration, and m^* = the effective mass[6]. Therefore, according to this equation, the effective masses of our title compounds can be evaluated as follows: 0.74, 0.80, 0.82, and 0.96 m_e for $Ca_9Zn_{4.5}Sb_9$, $Ca_8YbZn_{4.5}Sb_9$, $Ca_8YbZn_{4.4}Cu_{0.1}Sb_9$, and $Ca_8YbZn_{4.35}Cu_{0.15}Sb_9$, respectively. In addition, the effective mass and mobility are inversely proportional to each other, but those hardly affect *S* directly. Therefore, this kind of observation implied the possibility of multiple electronic bands or nonparabolic band effects, which could influence the TE properties of the title compounds. In addition, Supplementary Figure 4A displays the results for the power factor (*PF*), which was computed using $PF = S^2\sigma$.

Figure 8A shows the temperature-dependent thermal conductivity κ_{tot} of the title compounds with minimum κ_{tot} values of 0.57, 0.82, 0.76, 0.70, and 1.00 W/mK for $Ca_9Zn_{4.5}Sb_9$[19], $Ca_8YbZn_{4.5}Sb_9$, $Ca_8YbZn_{4.45}Cu_{0.05}Sb_9$, $Ca_8YbZn_{4.4}Cu_{0.1}Sb_9$, and $Ca_8YbZn_{4.35}Cu_{0.15}Sb_9$, respectively. Typically, the κ_{tot} is delineated as the sum of the electronic contribution κ_{elec} and the lattice contribution κ_{latt}. Given that the κ_{elec} value is determined through the application of the Wiedemann-Franz law ($\kappa_{elec} = L\sigma T$; $L = 1.5 + \exp[-\frac{|S|}{116}]$, where *L* is in 10^{-8} WΩK and S in μ/K), the determination of the term κ_{latt} involves the subtraction of the κ_{elec} from the κ_{tot} value ($\kappa_{latt} = \kappa_{tot} - \kappa_{elec}$)[32].

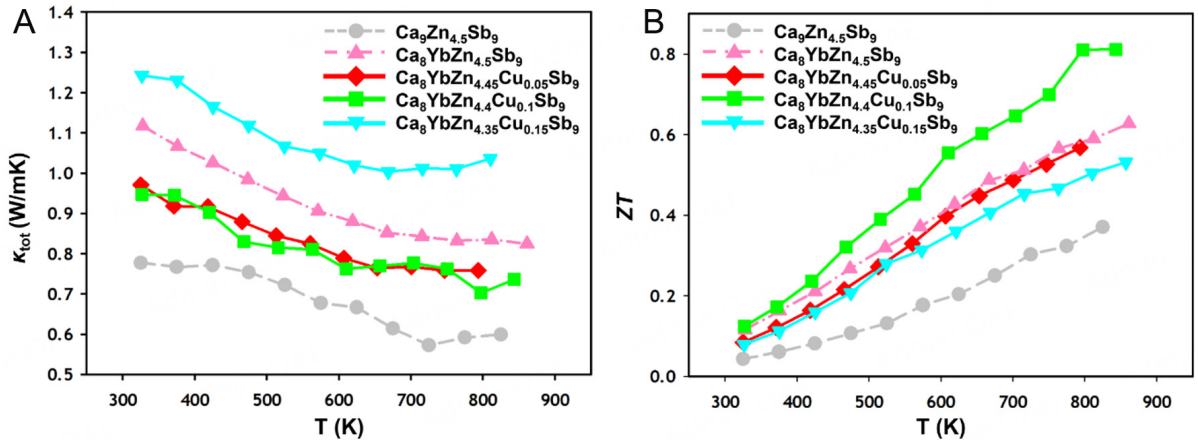

Figure 8. For four compounds in the $Ca_8YbZn_{4.5-y}Cu_ySb_9$ ($0 \le y \le 0.15$) system, temperature-dependent (A) total thermal conductivity κ_{tot} and (B) figure-of-merit *ZT* are plotted over the range of 323 to 861 K. Corresponding data for the ternary $Ca_9Zn_{4.5}Sb_9$[19] compound are presented for comparison.

The magnitude of κ_{tot} for the three co-substituted compounds exhibited decreasing patterns down to *ca*. 800 K. The expected decrease in κ_{tot} due to the increased phonon scattering caused by Yb substitution was contrary to expectations, as it increased compared to $Ca_9Zn_{4.5}Sb_9$. This should be attributed to the significantly increased κ_{elec} due to the enhancement in σ. Nevertheless, despite the increase in κ_{elec}, the κ_{tot} did not significantly increase in most of the $Ca_8YbZn_{4.5-y}Cu_ySb_9$ compounds, as κ_{latt} was reduced by the enhanced phonon scattering due to the Yb and Cu co-substitution. Based on this correlation, we have computed the κ_{elec} of 0.16, 0.28, 0.36, 0.27, and 0.27 W/mK at 325 K for $Ca_9Zn_{4.5}Sb_9$[19], $Ca_8YbZn_{4.5}Sb_9$, $Ca_8YbZn_{4.45}Cu_{0.05}Sb_9$, $Ca_8YbZn_{4.4}Cu_{0.1}Sb_9$, and $Ca_8YbZn_{4.35}Cu_{0.15}Sb_9$, respectively. The κ_{latt}, derived by subtracting κ_{elec} from κ_{tot}, is also presented in Supplementary Figure 4B.

Ultimately, the temperature-dependent *ZT* was calculated and displayed in Figure 8B. Overall, the *ZT* for all title compounds showed an increasing trend up to 861 K. Among these title compounds, $Ca_8YbZn_{4.4}Cu_{0.1}Sb_9$ attained a maximum *ZT* of 0.81 at 843 K, representing an improvement over the ternary parental compound $Ca_9Zn_{4.5}Sb_9$. In addition, the previously reported Cu-doped $Ca_9Zn_{4.35}Cu_{0.15}Sb_9$[38] showed a *ZT* of 0.72 at 873 K. Therefore, the highest *ZT* of our quaternary $Ca_8YbZn_{4.4}Cu_{0.1}Sb_9$ should be attributed to the enhanced σ and *S* resulting from the co-substitution of Yb and Cu compared to $Ca_9Zn_{4.5}Sb_9$. While the total thermal conductivity of $Ca_8YbZn_{4.4}Cu_{0.1}Sb_9$ displayed an increase in comparison to $Ca_9Zn_{4.5}Sb_9$, the enhanced σ was found to possess a disproportionately large influence over the overall TE properties.

CONCLUSIONS

A series of seven title compounds in the $Ca_{9-x}Yb_xZn_{4.5-y}Cu_ySb_9$ ($0 \le x \le 1.50$, $0 \le y \le 0.15$) system were prepared using the molten Pb-flux and hot-pressing method. Structural analyses revealed that all samples crystallized in the orthorhombic $Ca_9Mn_4Bi_9$-type structure (*Pbam* space group), as confirmed by PXRD and SXRD refinements. The chemical compositions were further validated through EDS and EPMA analysis, which also confirmed the partial substitutions Cu for Zn and Yb for Ca. Notably, the Zn1 site exhibited a partial occupancy with a relatively large ADP which was an intrinsic structural feature of this structure type. The structural refinement indicated that Yb displayed a specific site-preference for the A3 site, and this site-preference was attributed to the QVAL-based electronic factor rather than the size factor. Electronic

structure calculations using the TB-LMTO methods revealed that the *p*-type Cu doping indeed led to increased carrier concentrations and eventually to improved electrical conductivities. The ELF analysis further demonstrated that the Cu substitution altered the bond polarity within the anionic frameworks, improving carrier concentration and finally electrical conductivities. TE property measurements proved that the co-substitution of Yb and Cu significantly increased the σ compared to that of the parental compound $Ca_9Zn_{4.5}Sb_9$ despite the reduced carrier mobility. This observation demonstrated that the increased carrier concentration had a more significant effect on electrical conductivity than the decreased carrier mobility. The increase in σ also led to an enhancement in the κ_{elec}, which caused an overall increase in the κ_{tot}. However, the increase in phonon scattering by the Yb and Cu co-substitution resulted in the reduction in κ_{latt}, which suppressed the overall rise in κ_{tot}. As a result of these combinations, the optimized TE performance was achieved in $Ca_8YbZn_{4.4}Cu_{0.1}Sb_9$ with the maximum *ZT* of 0.81 computed at 843 K.

DECLARATIONS

Authors' contributions

Designed the experiment: Seo, N.; You, T. S.
Wrote the manuscript: Seo, N.; You, T. S.
Data analysis: Seo, N.; Lee, J.
Performed the physical characterization: Seo, N.; Lee, J.; Lee, Y.; Pi, J. H.; Lee, K. H.
Performed the SXRD measurements: Choi, M. H.; Ok, K. M.
Revised the manuscript: Lee, J.; You, T. S.
Acquired funding: Lee, K. H.; You, T. S.
Supervised students and developed concepts: You, T. S.

Availability of data and materials

The original supplementary crystallographic data for this study is openly available in the Cambridge Crystallographic Data Center (12 Union Road, Cambridge CB21EZ, UK; fax: +44-1223-336033) at www.ccdc.cam.ac.uk/data_request/cif (accessed on 10 February 2025), or by emailing data_request@ccdc.cam.ac.uk. The reference/accession number to be used is CCDC 2422809-2422812. Furthermore, the raw data supporting the conclusions of this article will be made available by the authors on request.

Financial support and sponsorship

This work was supported by the Basic Science Research Program through the National Research Foundation of Korea (NRF), funded by the Ministry of Science and ICT (RS-2024-00337629 and RS-2022-NR068194).

Conflicts of interest

All authors declared that there are no conflicts of interest.

Ethical approval and consent to participate

Not applicable.

Consent for publication

Not applicable.

REFERENCES

1. Qin, B.; Kanatzidis, M. G.; Zhao, L. D. The development and impact of tin selenide on thermoelectrics. *Science* **2024**, *386*, eadp2444. DOI
2. Jia, Y.; Jiang, Q.; Sun, H.; et al. Wearable thermoelectric materials and devices for self-powered electronic systems. *Adv. Mater.* **2021**, *33*, 2102990. DOI
3. Shuai, J.; Ge, B.; Mao, J.; Song, S.; Wang, Y.; Ren, Z. Significant role of Mg stoichiometry in designing high thermoelectric performance for $Mg_3(Sb,Bi)_2$-based n-type Zintls. *J. Am. Chem. Soc.* **2018**, *140*, 1910-5. DOI
4. Justl, A. P.; Ricci, F.; Pike, A.; et al. Unlocking the thermoelectric potential of the $Ca_{14}AlSb_{11}$ structure type. *Sci. Adv.* **2022**, *8*, eabq3780. DOI PubMed PMC
5. Justl, A. P.; Kauzlarich, S. M. Probing high-temperature oxidation of thermoelectric phases $Yb_{14}MSb_{11}$ (M = Mg, Mn, Zn). *ACS. Appl. Mater. Interfaces.* **2022**, *14*, 47246-54. DOI PubMed
6. Guo, K.; Cao, Q.; Zhao, J. Zintl phase compounds AM_2Sb_2 (A=Ca, Sr, Ba, Eu, Yb; M=Zn, Cd) and their substitution variants: a class of potential thermoelectric materials. *J. Rare. Earths.* **2013**, *31*, 1029-38. DOI
7. Jeong, J.; Shim, D.; Yox, P.; et al. Tuning the radius ratio to enhance thermoelectric properties in the Zintl compounds AM_2Sb_2 (A = Ba, Sr; M = Zn, Cd). *Chem. Mater.* **2023**, *35*, 3985-97. DOI
8. Lee, J.; Kim, M.; Pi, J. H.; et al. Insights into the crystal structure and thermoelectric properties of the Zintl phase $Ca_9Cd_{3+x-y}M_{x+y}Sb_9$ (M = Cu, Zn) system. *Chem. Mater.* **2025**, *37*, 368-77. DOI
9. Chen, C.; Xue, W.; Li, X.; et al. Enhanced thermoelectric performance of Zintl phase $Ca_9Zn_{4+x}Sb_9$ by beneficial disorder on the selective cationic site. *ACS. Appl. Mater. Interfaces.* **2019**, *11*, 37741-7. DOI
10. Bux, S. K.; Zevalkink, A.; Janka, O.; et al. Glass-like lattice thermal conductivity and high thermoelectric efficiency in $Yb_9Mn_{4.2}Sb_9$. *J. Mater. Chem. A.* **2014**, *2*, 215-20. DOI
11. Kazem, N.; Zaikina, J. V.; Ohno, S.; Snyder, G. J.; Kauzlarich, S. M. Coinage-metal-stuffed $Eu_9Cd_4Sb_9$: metallic compounds with anomalous low thermal conductivities. *Chem. Mater.* **2015**, *27*, 7508-19. DOI
12. Brechtel, E.; Cordier, G.; Schafer, H. Darstellung und kristallstruktur von $Ca_9Mn_4Bi_9$ und $Ca_9Zn_4Bi_9$/Preparation and crystal structure of $Ca_9Mn_4Bi_9$ and $Ca_9Zn_4Bi_9$. *Z. Naturforsch.* **1979**, *34*, 1229-33. DOI
13. Liu, X. C.; Wu, Z.; Xia, S. Q.; Tao, X. T.; Bobev, S. Structural variability versus structural flexibility. A case study of $Eu_9Cd_{4+x}Sb_9$ and $Ca_9Mn_{4+x}Sb_9$ ($x \approx 1/2$). *Inorg. Chem.* **2015**, *54*, 947-55. DOI
14. Liu, X. C.; Liu, K. F.; Wang, Q. Q.; Wang, Y. M.; Pan, M. Y.; Xia, S. Q. Exploring new Zintl phases in the 9-4-9 family via Al substitution. Synthesis, structure, and physical properties of $Ae_9Mn_{4-x}Al_xSb_9$ (Ae = Ca, Yb, Eu). *Inorg. Chem.* **2020**, *59*, 3709-17. DOI
15. Wang, Y.; Bobev, S. Rare-earth metal substitutions in $Ca_{9-x}RE_xMn_4Sb_9$ (*RE* = La-Nd, Sm; $x \approx 1$). Synthesis and characterization of a new series of narrow-gap semiconductors. *Chem. Mater.* **2018**, *30*, 3518-27. DOI
16. Smiadak, D. M.; Baranets, S.; Rylko, M.; et al. Single crystal growth and characterization of new Zintl phase $Ca_9Zn_{3.1}In_{0.9}Sb_9$. *J. Solid. State. Chem.* **2021**, *296*, 121947. DOI
17. Uvarov, C. A.; Ortega-Alvarez, F.; Kauzlarich, S. M. Enhanced high-temperature thermoelectric performance of $Yb_{14-x}Ca_xMnSb_{11}$. *Inorg. Chem.* **2012**, *51*, 7617-24. DOI PubMed
18. Shuai, J.; Wang, Y.; Liu, Z.; et al. Enhancement of thermoelectric performance of phase pure Zintl compounds $Ca_{1-x}Yb_xZn_2Sb_2$, $Ca_{1-x}Eu_xZn_2Sb_2$, and $Eu_{1-x}Yb_xZn_2Sb_2$ by mechanical alloying and hot pressing. *Nano. Energy.* **2016**, *25*, 136-44. DOI
19. Ohno, S.; Aydemir, U.; Amsler, M.; et al. Achieving zT > 1 in inexpensive Zintl phase $Ca_9Zn_{4+x}Sb_9$ by phase boundary mapping. *Adv. Funct. Mater.* **2017**, *27*, 1606361. DOI
20. APEX2, Version 2013.6-2. Madison, WI: Bruker AXS Inc., 2013.
21. SAINT. Madison, WI: Bruker AXS Inc., 2002.
22. Sheldrick, G. M. SADABS. Göttingen: University of Göttingen, 2003.
23. Gelato, L. M.; Parthé, E. *STRUCTURE TIDY* - a computer program to standardize crystal structure data. *J. Appl. Cryst.* **1987**, *20*, 139-43. DOI
24. Andersen, O. K. Linear methods in band theory. *Phys. Rev. B.* **1975**, *12*, 3060-83. DOI
25. Andersen, O. K.; Jepsen, O. Explicit, first-principles tight-binding theory. *Phys. Rev. Lett.* **1984**, *53*, 2571-4. DOI
26. Lambrecht, W. R. L.; Andersen, O. K. Minimal basis sets in the linear muffin-tin orbital method: application to the diamond-structure crystals C, Si, and Ge. *Phys. Rev. B. Condens. Matter.* **1986**, *34*, 2439. DOI
27. Jepsen, O.; Andersen, O. K. The STUTTGART TB-LMTO program. Available from: https://www2.fkf.mpg.de/andersen/LMTODOC/LMTODOC.html [Last accessed on 25 Jun 2025]
28. Andersen, O. K.; Jepsen, O.; Glötzel, D. Canonical description of the band structures of metals. 1985; pp. 65-72. Available from: https://www2.fkf.mpg.de/andersen/docs/pub/85CanonicalVarenna.pdf [Last accessed on 25 Jun 2025]
29. Jepsen, O.; Andersen, O. K. Calculated electronic structure of the sandwichd^1 metals LaI_2 and CeI_2: application of new LMTO techniques. *Z. Physik. B. Condensed. Matter.* **1995**, *97*, 35-47. DOI
30. Blöchl, P. E.; Jepsen, O.; Andersen, O. K. Improved tetrahedron method for Brillouin-zone integrations. *Phys. Rev. B. Condens. Matter.* **1994**, *49*, 16223-33. DOI PubMed
31. Borup, K. A.; de Boor, J.; Wang, H.; et al. Measuring thermoelectric transport properties of materials. *Energy. Environ. Sci.* **2015**, *8*, 423-35. DOI

32. Kim, H.; Gibbs, Z. M.; Tang, Y.; Wang, H.; Snyder, G. J. Characterization of Lorenz number with Seebeck coefficient measurement. *APL. Mater.* **2015**, *3*, 041506. DOI
33. Xia, S. Q.; Bobev, S. Interplay between size and electronic effects in determining the homogeneity range of the $A_9Zn_{4+x}Pn_9$ and $A_9Cd_{4+x}Pn_9$ phases (0 < or = x < or = 0.5), A = Ca, Sr, Yb, Eu; Pn = Sb, Bi. *J. Am. Chem. Soc.* **2007**, *129*, 10011-8. DOI
34. Bobev, S.; Thompson, J. D.; Sarrao, J. L.; Olmstead, M. M.; Hope, H.; Kauzlarich, S. M. Probing the limits of the Zintl concept: structure and bonding in rare-earth and alkaline-earth zinc-antimonides $Yb_9Zn_{4+x}Sb_9$ and $Ca_9Zn_{4.5}Sb_9$. *Inorg. Chem.* **2004**, *43*, 5044-52. DOI PubMed
35. Shannon, R. D. Revised effective ionic radii and systematic studies of interatomic distances in halides and chalcogenides. *Acta. Cryst. A.* **1976**, *32*, 751-67. DOI
36. Wachter, J. The Elements. Von J. Emsley. Clarendon Press, Oxford 1989. 256 S., Paperback £ 9.95. – ISBN 0-19-855237-8. *Angew. Chem. Int. Ed.* **1990**, *102*, 115. DOI
37. Lei, J.; Wuliji, H.; Zhao, K.; et al. Efficient lanthanide Gd doping promoting the thermoelectric performance of Mg_3Sb_2-based materials. *J. Mater. Chem. A.* **2021**, *9*, 25944-53. DOI
38. Wu, Z.; Li, J.; Li, X.; et al. Tuning the thermoelectric properties of $Ca_9Zn_{4+x}Sb_9$ by controlled doping on the interstitial structure. *Chem. Mater.* **2016**, *28*, 6917-24. DOI